



Cardiac MR Elastography Using Reduced-FOV, Single-Shot, Spin-Echo EPI

Yi Sui ¹, Shivaram P. Arunachalam ¹, Arvin Arani,¹ Joshua D. Trzasko,¹ Phillip M. Young,¹ James F. Glockner,¹ Kevin J. Glaser,¹ David S. Lake,² Kiaran P. McGee,¹ Armando Manduca,² Phillip J. Rossman,¹ Richard L. Ehman,¹ and Philip A. Araoz^{1*}

Purpose: To implement a reduced field of view (rFOV) technique for cardiac MR elastography (MRE) and to demonstrate the improvement in image quality of both magnitude images and post-processed MRE stiffness maps compared to the conventional full field of view (full-FOV) acquisition.

Methods: With Institutional Review Board approval, 17 healthy volunteers underwent both full-FOV and rFOV cardiac MRE scans using 140-Hz vibrations. Two cardiac radiologists blindly compared the magnitude images and stiffness maps and graded the images based on several image quality attributes using a 5-point ordinal scale. Fisher's combined probability test was performed to assess the overall evaluation. The octahedral shear strain-based signal-to-noise ratio (OSS-SNR) and median stiffness over the left ventricular myocardium were also compared.

Results: One volunteer was excluded because of an inconsistent imaging resolution during the exam. In the remaining 16 volunteers (9 males, 7 females), the rFOV scans outperformed the full-FOV scans in terms of subjective image quality and ghosting artifacts in the magnitude images and stiffness maps, as well as the overall preference. The quantitative measurements showed that rFOV had significantly higher OSS-SNR (median: 1.4 [95% confidence interval (CI): 1.2–1.5] vs. 2.1 [95% CI: 1.8–2.4]), $P < 0.05$) compared to full-FOV. Although no significant change was found in the median myocardial stiffness between the 2 scans, we observed a decrease in the stiffness variation within the myocardium from 2.1 kPa (95% CI: [1.9, 2.3]) to 1.9 kPa (95% CI: [1.7, 2.0]) for full-FOV and rFOV, respectively ($P < 0.05$) in a subgroup of 7 subjects with ghosting present in the myocardium.

Conclusion: This pilot volunteer study demonstrated that rFOV cardiac MRE has the capability to reduce ghosting and to improve image quality in both MRE magnitude images

and stiffness maps. **Magn Reson Med 80:231–238, 2018.**
© 2017 The Authors Magnetic Resonance in Medicine published by Wiley Periodicals, Inc. on behalf of International Society for Magnetic Resonance in Medicine. This is an open access article under the terms of the Creative Commons Attribution NonCommercial License, which permits use, distribution and reproduction in any medium, provided the original work is properly cited and is not used for commercial purposes.

Key words: reduced FOV; cardiac MRE; MR elastography; myocardial stiffness

INTRODUCTION

Cardiac magnetic resonance elastography (MRE) is emerging as a valuable noninvasive imaging tool for assessing the biomechanical properties of myocardial tissues (1–5). A single-shot, spin-echo, echo-planar imaging (SS-SE-EPI) pulse sequence is often used for cardiac MRE because of its fast imaging speed and insensitivity to cardiac motion (6). However, SS-SE-EPI-based cardiac MRE is still vulnerable to geometric distortion and ghosting from a variety of sources including susceptibility, chemical shift, in-plane flow, cardiac motion, and echo-misalignment. In particular, Nyquist N/2 ghosting is one of the most common artifacts caused by induced eddy currents, concomitant gradient fields, and relative delays of the physical x, y, and z gradients (7–9). These issues are further complicated by anisotropic gradient delays in oblique scan planes (10,11), which are routinely used in cardiac MRE when acquiring short-axis and long-axis views.

Cardiac MRE has to use symmetric k-space coverage because of the large local phase variations from the MRE motion-encoding gradients (MEGs), which leads to lower signal-to-noise ratio (SNR) compared to the conventional, magnitude-only cardiac MRI that uses partial-Fourier acquisitions to reduce the echo time (TE). Parallel imaging using sensitivity encoding (SENSE) (12) can be applied to reduce the TE and image distortion by shortening the EPI echo train length. However, SENSE-based scan acceleration also amplifies noise and ghosting because of the reduced amount of data used during image reconstruction and oversimplifications in standard reconstruction models. Although several sophisticated methods have been proposed to suppress residual Nyquist ghosting (10,13,14), which is partially mitigated via reference-scan-based phase correction (15), they

¹Department of Radiology, Mayo Clinic, Rochester, Minnesota, USA.

²Department of Physiology and Biomedical Engineering, Mayo Clinic, Rochester, Minnesota, USA.

Grant sponsor: National Institute of Health; Grant number: R01_HL115144.

*Correspondence to: Phillip A. Araoz, Professor of Diagnostic Radiology, College of Medicine, Department of Radiology, Mayo Clinic, 200 First Street SW, Rochester, MN 55905. E-mail: paraoz@mayo.edu

Kevin Glaser, Kiaran McGee, Armando Manduca, Richard L. Ehman and the Mayo Clinic have intellectual property rights and financial interests in some of the technology used in this study.

Received 11 April 2017; revised 29 October 2017; accepted 9 November 2017

DOI 10.1002/mrm.27029

Published online 1 December 2017 in Wiley Online Library (wileyonlinelibrary.com).

© 2017 The Authors Magnetic Resonance in Medicine published by Wiley Periodicals, Inc. on behalf of International Society for Magnetic Resonance in Medicine. This is an open access article under the terms of the Creative Commons Attribution NonCommercial License, which permits use, distribution and reproduction in any medium, provided the original work is properly cited and is not used for commercial purposes.

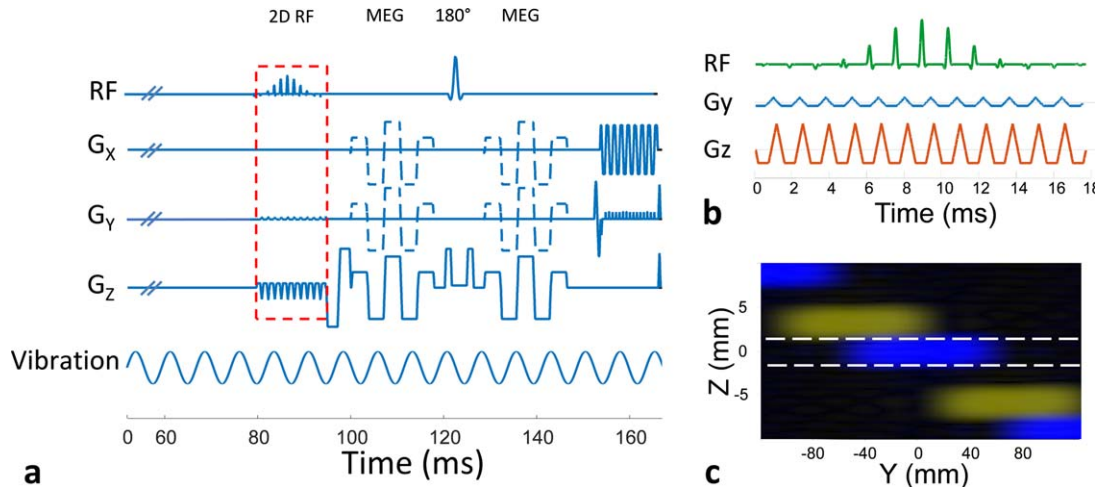


FIG. 1. (a) The timing diagram for the ECG-gated, SE-EPI, cardiac MRE pulse sequence with 2D RF excitation, (b) the custom-designed 2D RF excitation pulse, and (c) its simulated excitation profile showing the location of water (blue) and lipid (yellow) signals. Only the water signal is refocused by the subsequent slice-selective 180° pulse in the SE-EPI pulse sequence (dashed line).

typically require off-line reconstruction and are not currently viable for the routine clinical use.

Earlier studies have shown that combining a 2D spatially selective excitation (16–18) and a reduced field of view (rFOV) along the phase-encoding direction could be an effective approach for reducing ghosting in abdominal MRE (19). The rFOV technique is particularly well-suited for a targeted anatomic region such as the heart, as the peripheral body region is not excited by the 2D pulse, therefore eliminating the source of ghosting. The purpose of this study was to determine if a rFOV technique can qualitatively and quantitatively improve the image quality of cardiac MRE magnitude images and postprocessed stiffness maps compared to the conventional full field of view (full-FOV) acquisition in healthy volunteers.

METHODS

Imaging Sequence

In this study, we implemented a custom, 2D, echo-planar excitation, radiofrequency (RF) pulse into a SS-SE-EPI cardiac MRE sequence (Fig. 1a). In this RF design, the side excitation bands were tilted away from the imaging volume to avoid unwanted saturation of nearby slices (20,21). The 2D RF excitation pulse was designed using a tilted excitation by rotating the trajectory of excitation k -space in the (k_y, k_z) -plane as described in previous studies (17,20,21), where k_y and k_z denote the phase- and slice-encoding directions, respectively. A fly-back EPI gradient (20) was used along the slice-selection direction to eliminate the sensitivity to RF/gradient timing errors that can result in Nyquist ghosts between the excitation bands (Fig. 1b). This is analogous to the Nyquist ghosting caused by bipolar readout gradients in SS-EPI acquisitions. The width of the fly-back gradient lobes was minimized by using the maximum slew rate allowed without inducing peripheral nerve stimulation (22).

Each RF subpulse, which determines the segment selection along the phase-encoding direction, was designed

using a linear-phase Shinnar-Le Roux (SLR) method (23) with a time-bandwidth product (TB) of 4 (i.e., bandwidth = 5.7 kHz and pulse width = 0.7 ms) and 1% pass- and stop-band ripples (19). Thirteen subpulses separated with a time delay of 0.7 ms (to allow for the gradient fly-back pulses) were concatenated under an envelope pulse, which determines the slice selection. The envelope pulse was also designed using a linear-phase SLR method with the following parameters: TB = 4, pulse width = 17.5 ms, in/out of slice ripple = 1%.

Simultaneous lipid suppression with the 2D RF pulse was achieved in 2 steps. First, the duration between any 2 consecutive subpulses was carefully selected so that the lipid signal (the yellow areas in Fig. 1c) was shifted completely outside of the water profile (the blue areas in Fig. 1c). Second, similar to the slice-selection gradient-reversal method (24), the subsequent slice-selective 180° pulse in the SE-EPI pulse sequence was designed to have an opposite spatial shift of the lipid along the slice-selection direction to make the lipid signal not refocusable. In contrast, the 180° pulse adequately refocused the water signal in the targeted slice (central blue area in Fig. 1c). The 2D spatial response of the 2D RF pulse, as well as the different responses of water and lipids (220 Hz chemical shift at 1.5T), were analyzed using the Bloch equations with customized simulation programs written in MATLAB (The MathWorks, Natick, MA).

This 2D RF pulse was implemented into a SS-SE-EPI MRE sequence. The slice locations and orientation can be adjusted as needed during the exam. The MEGs are 1^{st} -moment-nulled, oscillating at the same frequency as the external vibration (Fig. 1a). The motion was started 100-ms before the start of the MEGs to allow the motion to propagate into the heart and approach a steady state after each cardiac trigger.

Study Population

With Institutional Review Board approval, 17 healthy volunteers with no history of heart diseases or diabetes were enrolled in this prospective study, and written

Table 1
MRE Scan Parameters

Scan Parameters	Full FOV	rFOV
TE (ms)	68.7	71.3
TR (ms)	variable ^a	variable ^a
FOV (mm)	320	320
Phase FOV (%)	100	50
Matrix	64 × 64	64 × 32
Slice thickness (mm)	5	5
No. of slices	5	5
Acceleration factor	2	1

Abbreviations: FOV, field of view; MRE, magnetic resonance elastography; TE, echo time; TR, pulse repetition time.

^aTRs were matched to 5 RR intervals according to each volunteer's heart rate.

informed consent was received from each subject. All subjects underwent cardiac MRI/MRE scans.

MRE Acquisition

MRI scans were conducted on a clinical 1.5T wide-bore MR scanner (Optima MR450W, GE Healthcare, Milwaukee, WI) with a receive-only, integrated, whole-body phased array coil (geometry embracing method [GEM] anterior–posterior array, GE Healthcare). The vibrations were generated using a high-power, pneumatic, active driver and a customized, passive, drum driver for the heart (25). The imaging procedure was the same as described in previous studies (26). Both full-FOV and rFOV cardiac MRE were performed in an oblique imaging plane to obtain short-axis images of the heart using 140-Hz vibrations, 2 MEG pairs, 3 motion-encoding directions plus 1 no-motion scan, and 4 phase offsets spaced evenly over 1 period of the vibration. Images were acquired at the minimum MR sequence delay in the cardiac cycle (~100 ms) after the R-wave ECG trigger. The repetition time (TR) was matched to the volunteer's heart rate with ECG gating. The total scan time was ~84 s with 4 breath holds.

The scan parameters are shown in Table 1. The pulse width of the 2D RF in the rFOV sequence was slightly longer than the spatial-spectral (SPSP) pulse used in the full-FOV sequence, resulting in a small difference (2.5 ms) in the TEs. A 50% phase FOV was used in the rFOV scans and the acquisition matrix was also halved along the phase direction in the rFOV scans to match the resolution of the full-FOV scans. Five slices were acquired across 5 RR intervals. The standard SENSE-type parallel imaging technique (ASSET: array coil spatial sensitivity encoding technique, GE Healthcare, Waukesha, WI) was used for the full-FOV acquisitions with an acceleration factor of 2. No acceleration was used for the rFOV acquisitions to gain SNR by reducing the g-factor. In the ASSET method, the coil sensitivity maps were obtained from a separate calibration scan using a low-resolution, 2D, fast-gradient-echo sequence. Extrapolation of the sensitivity maps is also used to further reduce the effects of patient motion and edge effects (27).

MRE Stiffness Maps

MRE stiffness maps were generated by calculating the curl of the 3D displacement field (28) and then

performing a 3D local frequency estimation (LFE) of the curl data to invert the wave field and calculate the stiffness maps (elastograms) (25,26,29).

Qualitative Image Evaluation

The exams were qualitatively reviewed by 2 board-certified radiologists experienced in cardiac imaging and MRE. Each pair of MRE magnitude images and postprocessed stiffness maps were compared in a blinded, randomized fashion. The full-FOV images were cropped to have the same apparent FOV as the rFOV images and were randomly assigned to be the first or second image in the pair.

The image pairs were graded on a 5-point ordinal scale from –2 to +2, with –2 indicating a strong preference for the first image, +2 indicating a strong preference for the second image, and 0 representing no preference (30). The order of the rFOV and full-FOV images in the pair was blinded to the readers. The scores were then adjusted to reflect that +2 indicates a strong preference for the rFOV images. In other words, if the first image in the pair was assigned to be the rFOV image, the opposite value of its score would be used for the statistical analysis.

For magnitude images, the following attributes were compared: subjective image quality, ghosting artifact level, and blood suppression. For the stiffness maps, only subjective image quality and ghosting artifact level were used. The readers then gave an overall preference for the compared pair.

One-sided, Wilcoxon, signed-rank tests were performed to assess if there was a significant improvement between the 2 techniques in each category. The null hypothesis of the left-sided test was that the rFOV images performed equally to or better than the standard full-FOV images, and the right-sided test used the reverse of this hypothesis. Fisher's combined probability test was then used to combine the evaluation of the two radiologists. A *P*-value below 0.05 was considered to be significant.

Because ghosting in the myocardium has a larger impact on the myocardial stiffness calculation than ghosting elsewhere in the images, we also assessed the location of the ghosting using 3 categories: (1) no ghosting observed, (2) ghosting overlapped the myocardium, and (3) ghosting outside of myocardium.

Quantitative Image Evaluation

The myocardial regions of interest (ROIs) were drawn by manually tracing the left ventricular (LV) endocardial and epicardial contours using commercially available software (cvi42, Circle Cardiovascular Imaging, Calgary, AB, Canada). The LV endocardium and epicardium were manually traced on magnitude images and were copied onto the stiffness maps.

Octahedral-shear-strain-based signal-to-noise ratio (OSS-SNR) measured in the myocardial ROIs was used as a quantitative image quality parameter. The octahedral shear strain (OSS) is the maximum strain in any plane for a 3D strain state, and the OSS-SNR compares this shear strain to the strain noise calculated from the residual of the least-squares fitting of a sinusoid to the four measured phase offsets of the MRE curl images (31). The

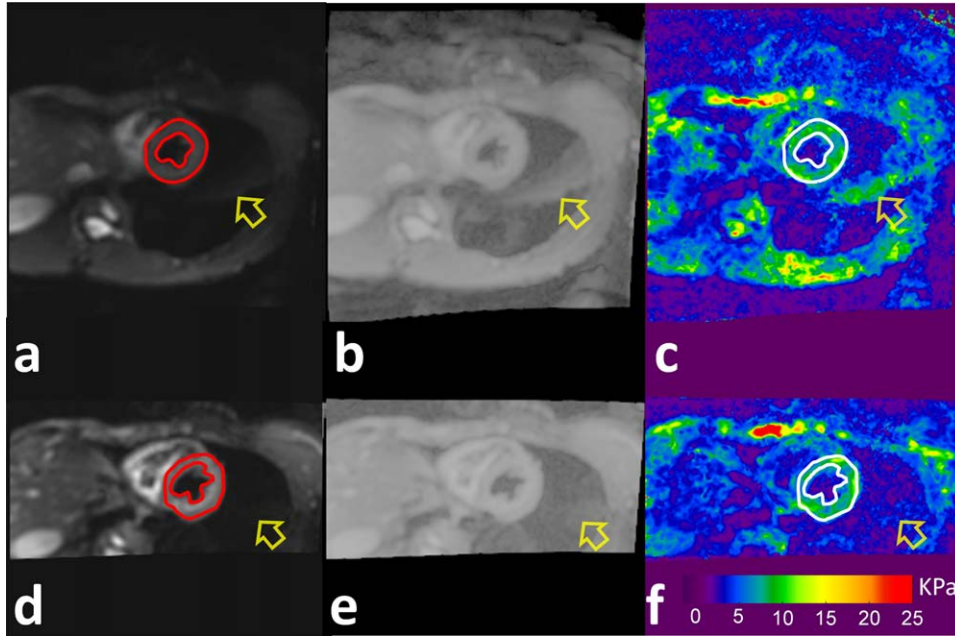


FIG. 2. Representative comparison between the full-FOV (top row) and the reduced-FOV (rFOV) technique (bottom row) showing magnitude images (a,d), the corresponding log-scaled images (b,e) to highlight the ghosting, and stiffness maps (c,f). Yellow arrows indicate the ghosting that was significantly reduced when using the rFOV technique. The red contours show the LV endocardium and epicardium ROIs that were manually traced on the magnitude images and copied onto the stiffness maps.

OSS-SNR was calculated using custom software written in MATLAB.

In addition to these quality metrics, the median myocardial stiffness within the left ventricular mask was measured using the ROIs from all 5 slices to determine if the overall myocardial stiffness measurements varied between the rFOV and full-FOV stiffness maps. To further evaluate the ghosting effects on the myocardial stiffness calculation, we took a subgroup of the exams that exhibited ghosting in the myocardium in either the full-FOV or rFOV scans and compared the median values and variations of the stiffness within the myocardial ROIs.

The OSS-SNR and median myocardial stiffness were compared between the full-FOV and rFOV using one-sided, Wilcoxon, signed-rank tests like above. A P -value below 0.05 was considered to be significant.

RESULTS

2D Spatially Selective RF Pulse Design

The waveforms for the designed 2D RF pulse and gradients are shown in Figure 1b. The simulation result (Fig. 1c) confirmed the performance of the 2D RF pulse. It shows the tilted spatial response profiles in the (y,z)-plane, as designed, removing the limitation of the number of slices in the multislice acquisition. For our MRI system with a maximum gradient amplitude of 34 mT/m, the minimum slice thickness and phase FOV were limited as 4 mm and 40 mm, respectively. The lipid signal (yellow) was also shifted away from the center of the water lobe by the slice thickness (5 mm for this study), enabling lipid suppression when a subsequent 180° pulse is applied. The lipid suppression was confirmed

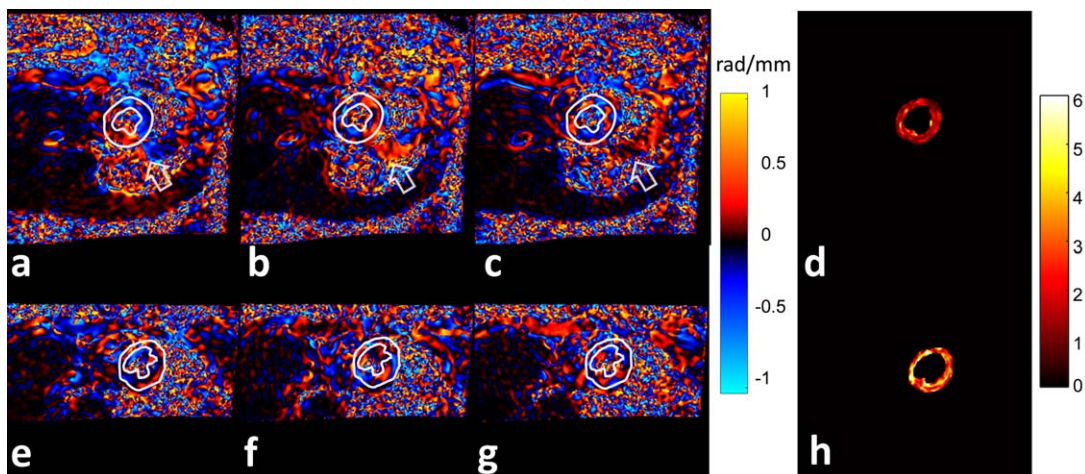
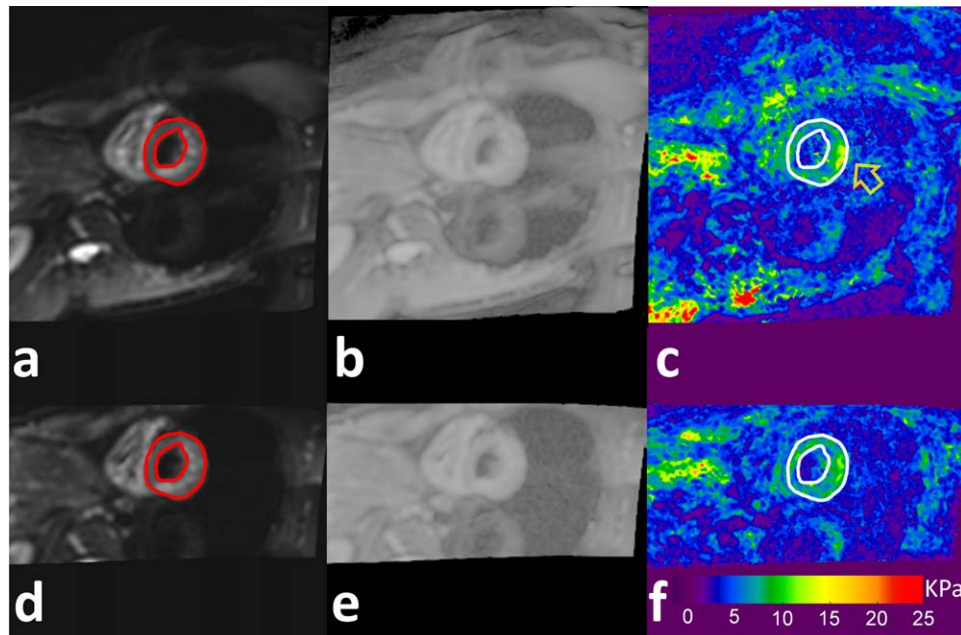


FIG. 3. Example curl wave field images from the same subject as shown in Figure 2. (a,e) x, (b,f) y, and (c,g) z components of the curl field from the full-FOV (top row) and the rFOV (bottom row) scans. The ghosting (white arrows) in the full-FOV scans overlapped the LV wall (white contours) and contaminated the waves. The masked OSS-SNR maps (d,h) showed increased wave quality in the LV wall in the rFOV images.

FIG. 4. A representative case comparing the ghosting level in the myocardium (red and white contours) between the full-FOV (top row) and rFOV techniques (bottom row) including magnitude images (a,d), the corresponding log-scaled images (b,e) to highlight the ghosting, and the stiffness maps (c,f). The full-FOV scan exhibits an artefactual hotspot in the stiffness map (arrow in c) arising from the severe ghosting. In contrast, the rFOV technique substantially reduced the ghosting, hence resulting in a more homogenous stiffness map of the myocardium.



on a fat-water phantom, and the residual lipid signal was below 7% of its original value.

Study Population

One of the 17 volunteers was excluded because of an inconsistent imaging resolution used during the MRI acquisition. The remaining 16 volunteers (9 males, 7 females) had a median age of 24.5 years old (range: 22–35), median weight of 71.4 kg (range: 52.2–104), median height of 171 cm (range: 157–188), and median body-mass index of 23.1 kg/m² (range: 18.6–37.1).

Representative Comparison

Figure 2 shows a representative comparison between the full-FOV (top row) and rFOV techniques (bottom row). The ghosting artifacts (yellow arrows) in the rFOV scans was significantly reduced on the magnitude images

(Figs. 2a and 2d), the corresponding log scale images (Figs. 2b and 2e), and the calculated stiffness maps (Figs. 2c and 2f). The LV endocardium and epicardium were manually traced on the magnitude images (red contours in Figs. 2a and 2d), and were copied onto the stiffness maps (white contours in Figs. 2c and 2f).

Figure 3 shows the curl of the measured vector wave images from the same subject as in Figure 2. The first phase offset of the (Figs. 3a and 3d) x, (Figs. 3b and 3e) y, and (Figs. 3c and 3f) z components of the curl vector were compared between the full-FOV (top row) and rFOV (bottom row) scans. It can be observed that part of the ghosting (white arrows) in the full-FOV scans overlapped the heart region (white contours) and contaminated the LV waves, whereas the ghosting was suppressed in the rFOV results. The myocardial OSS-SNR maps (Figs. 3d and 3h) showed increased wave quality (higher OSS-SNR) in the LV wall in the rFOV images.

FIG. 5. The qualitative evaluation with pooled histograms of each of the 6 image characteristics as shown in the titles. Fisher’s combined probability test was performed on the scores from the 2 readers (blue and yellow). The score -2 indicates a strong preference for the full-FOV images and +2 a strong preference for the rFOV images. The significance results of the right-tailed tests are included with each histogram.

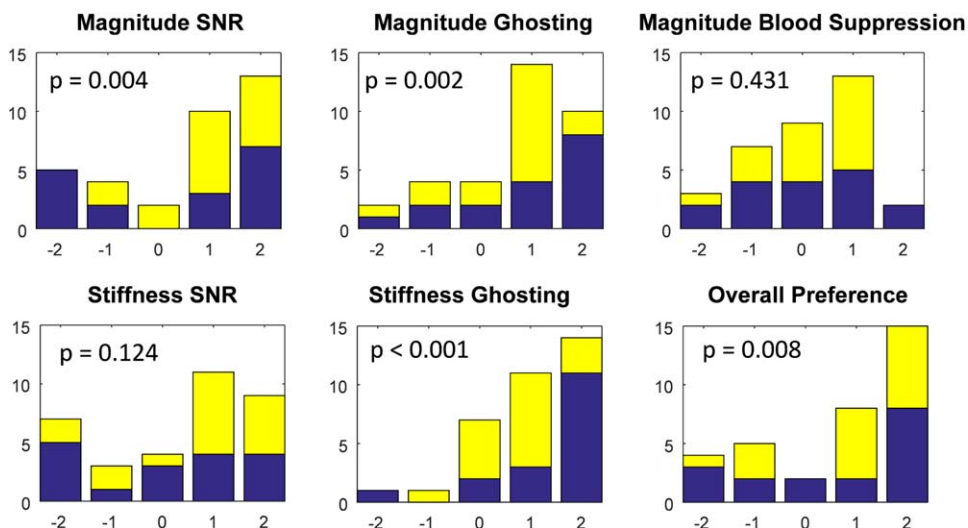


Table 2
Locations of Ghosting Observed in the Full-FOV and rFOV Scans

	Ghosting in	Ghosting outside	No Ghosting	Total
	Myocardium	Myocardium	Observed	
Full FOV	7	9	0	16
rFOV	2	1	13	16

Abbreviations: FOV, field of view.

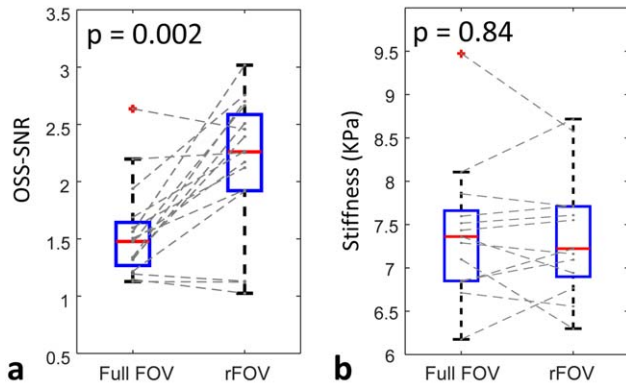


FIG. 6. Boxplots of the quantitative comparisons between the (a) OSS-SNR and (b) stiffness of the full-FOV and rFOV acquisitions. The box represents data from the 25th to 75th percentiles; the red line represents the median value; and dashed lines extend from the box to the 10th and 90th percentiles. The right-sided Wilcoxon, sign-rank test was performed on the OSS-SNR data, and the 2-sided test was performed on the stiffness data. The dashed lines link the data points from the same volunteer.

Figure 4 shows another representative case where the full-FOV scan exhibits an artefactual hotspot in the stiffness map arising from the severe ghosting. In contrast, the rFOV technique substantially reduced the ghosting, which resulted in a more homogenous stiffness map of the myocardium in the healthy volunteer.

Qualitative Evaluation

The rFOV scans outperformed the full-FOV scans on multiple qualitative measures. Figure 5 summarizes the results of the qualitative evaluation, with pooled histograms for each of the 6-image quality criteria. Fisher’s combined probability test was performed on the scores from the 2 readers. The significant results of the right-tailed test are shown on the histograms.

At a 5% significance level, the right-sided test results indicate that the rFOV scans outperformed the full-FOV scans in terms of subjective magnitude quality, magnitude ghosting artifact level, stiffness map ghosting

artifact level, and overall preference, although not in magnitude blood suppression and stiffness subjective image quality. All left-sided tests also failed to reject the null hypothesis, indicating that the rFOV scans did not perform worse than the full-FOV scans with respect to these latter 2 quantities.

The locations of the ghosting are summarized in Table 2. We observed that all full-FOV scans had ghosting and 7 of them overlapped the myocardium. In contrast, only 3 rFOV scans had ghosting and only 1 of them occurred in the myocardium.

Quantitative Evaluation

The rFOV scans outperformed the full-FOV scans according to the OSS-SNR measures. The boxplot of the OSS-SNR differences is shown in Figure 6a. Compared to the full-FOV scans, 12 of the 16 rFOV scans showed increased OSS-SNR (median: 1.4 [95% CI: 1.2–1.5] vs. 2.1 [95% CI: 1.8–2.4]). At a 5% significance level, the right-sided, Wilcoxon, sign-rank test suggested the OSS-SNR from rFOV were significantly higher than that of full-FOV ($P < 0.05$, $Z = 2.82$).

Three volunteers had OSS-SNR lower than an empirical threshold of 1.2, indicating unreliable stiffness estimation on these subjects (25). Therefore, they were excluded from the stiffness comparison. In the remaining 13 subjects, no significant difference was found in the median myocardial stiffness between the full-FOV and rFOV images (median: 7.4 kPa [95% CI: 6.9–7.6 kPa] vs. 7.2 kPa [95% CI: 6.9–7.7 kPa] respectively). Figure 6b compares the myocardium stiffness calculated from the full-FOV and rFOV scans, and no significant change was found using a 2-sided, Wilcoxon, sign-rank test ($P = 0.84$).

We further compared the stiffness in the cohort of those 7 volunteers with ghosting in the myocardium. The results were shown in Table 3. Though there was no significant difference in the stiffness between full-FOV (median: 7.0 kPa [95% CI: 6.2–7.4 kPa]) and rFOV (median: 6.8 [95% CI: 6.6–7.6 kPa], $P = 0.81$), we did observe a decrease in the stiffness variation within the myocardial ROIs from 2.1 kPa (95% CI: 1.9–2.3 kPa) to 1.9 kPa (95% CI: 1.7–2.0 kPa) for full-FOV and rFOV respectively ($P < 0.05$), indicating the stiffness maps calculated from the rFOV acquisitions were more stable.

DISCUSSION

To the best of our knowledge, this is the first study to demonstrate the feasibility of using a rFOV technique to improve image quality in cardiac MRE. The rFOV scans outperformed the full-FOV scans with reduced ghosting artifacts and higher MRE wave quality (OSS-SNR).

Table 3
Median Stiffness and Variation within the Myocardium ROIs in the 7 Volunteers With Ghosting in Myocardium

	Median Stiffness (kPa)	Stiffness Variation (kPa)
Full FOV	7.0 (range: 6.1–8.1) 95% CI: [6.2 7.4]	2.1 (range: 1.7–2.3) 95% CI: [1.9 2.3]
rFOV	6.8 (range: 6.1–8.7) 95% CI: [6.6 7.6]	1.9 (range: 1.7–2.2) 95% CI: [1.7 2.0]
<i>P</i>	0.81	<0.05

Abbreviations: CI, confidence interval; FOV, field of view; ROIs, regions of interest.

In cardiac MRE, the ghosting artifacts that occur in the myocardium could contaminate the MRE wave fields and result in artefactual stiffness values in the contaminated regions (such as the hotspot shown in Fig. 4). These hotspots would have a higher change to be misinterpreted as lesions in patients with conditions like myocardial infarction or amyloidosis that are known to have stiffer myocardium (26,32). In this study, we have demonstrated that the proposed rFOV technique is able to largely reduce the ghosting artifacts and therefore avoid the hotspots in the stiffness maps caused by the ghosting. Therefore, this rFOV technique has the benefit of minimizing the risk of misinterpretation of clinical cardiac MRE images.

The ghosting in cardiac MRE typically originates from the body wall at the peripheries of the FOV (Fig. 2), where the $N/2$ Nyquist ghost due to EPI echo misalignment is usually worse. This is especially likely in arbitrary, double-oblique scan planes because of eddy currents, B_0 field inhomogeneity, and concomitant field effects. Hence, when applying 2D spatially selective RF pulses in the proposed rFOV technique, the outer volume is not excited, leaving no signal to produce ghosts. It should also be noted that this rFOV implementation is readily available for clinical use as it uses the exact same reconstruction method as conventional EPI-based MRI scans.

There are other approaches that have been developed to reduce these ghosting artifacts. Several sophisticated correction methods based on SENSE (10,13,14) have been proposed to reduce ghosting levels, but they typically require an extensive off-line reconstruction and long computation time. A saturation band can also be placed over the posterior body wall to suppress ghosting. However, the saturation pulse may be less effective if off-resonance effects are large. In addition, a saturation pulse may prolong the minimum cardiac delay time allowed.

Another advantage of this rFOV method is that it enables TE shortening without requiring parallel imaging. In our study, parallel imaging acceleration was not used for the rFOV scan although we kept the same echo train length and similar TE as the full-FOV scans with an acceleration factor of two. This helped to improve the SNR in the rFOV scans by avoiding the noise amplification associated with parallel imaging. Of course, even greater scan time reduction can be achieved by combining the proposed rFOV strategy and parallel imaging, albeit with an expected SNR loss. It could be beneficial to measure the g-factors at different combinations of FOV reduction and parallel acceleration factors. The practical advantages and disadvantages of this combination study will be characterized in our future work.

One drawback of this tilted 2D RF design is that it has a higher specific absorption rate (SAR) than regular 2D RF or spatial-spectral pulses (21). With the protocol used in this study (TR of ~ 5 s measuring 5 slices), the average SAR reported by the scanner for the full-FOV and the rFOV scans are 0.030 W/kg and 0.037 W/kg, respectively. Though the average SAR for rFOV MRE was 23% higher than for full-FOV MRE, both methods have a much lower SAR than the FDA limits (2 W/kg for body).

In this study, the phase FOV (160 mm) was set to be 50% of the readout FOV based on 2 considerations. First, the heart may be significantly larger in patients with certain diseases and we would like to set an appropriate FOV window that will fit all volunteers and future patients. Second, the MRE inversion algorithm for calculating stiffness involves curl and Laplacian operators that have a footprint of 3 pixels (~ 15 mm with the 5-mm resolution used in this study). Therefore, it is necessary to leave sufficient space between the heart and the edge of the image to ensure the accuracy of the stiffness calculations within the myocardium.

In our study, 3 subjects were found to have low OSS-SNR (< 1.2) for both the full-FOV and rFOV acquisitions (Fig. 5b). Further investigation revealed that the curl wave amplitude was low in all 3 cases, and large motion was also observed between different MRE phase offsets. This may result from a number of possible factors including poor ECG gating, inconsistent breath holds, and potentially inadequate wave penetration into the myocardium.

Although this study was the first to demonstrate the feasibility of performing rFOV cardiac MRE, a previous study did propose using rFOV methods to reduce the scan time in non-cardiac MRE applications (33). In that study, rFOV MRE and 1D MRE (beam MRE) were performed using spiral 2D spatially selective RF excitations for gradient-echo (GRE) applications and intersecting 90° and 180° slice-selective excitations for spin-echo (SE) applications. This approach may not be suitable for cardiac EPI-based MRE because it does not provide multislice capability and fat saturation, which are required for clinical cardiac scans. A cardiac DTI study was performed with reduced phase FOV acquisitions using a spin-echo sequence with a tilted refocusing RF pulse to achieve multislice imaging and fat saturation (34). However there has to be a gap between slices because of the tilted refocusing pulse used. This slice gap would hinder the 3D MRE inversion algorithm used in this study, which requires continuous slices. The rFOV technique used in this study does not have this limitation.

Our study has several limitations. First, we were unable to use a true background noise estimate for quantifying the SNR of the myocardium. Therefore, our quantitative comparison was calculated based on a phase-derived OSS-SNR. Second, only a small number of healthy volunteers were included in this preliminary study. Although we showed no difference in the mean stiffness between the rFOV and full-FOV scans, future studies on cardiac patients are vital to verify if the rFOV method can provide a more accurate measure of the stiffness in patients with various pathologies and if it can help to improve diagnostic accuracy.

CONCLUSION

This study demonstrated that SS-SE-EPI-based cardiac MRE using reduced-FOV techniques is valuable in reducing ghosting artifacts and improving image quality in healthy volunteers. Further validation on cardiac patients will help our understanding of the potential clinical benefits of reduced-FOV cardiac MRE.

REFERENCES

- Kolipaka A, Araoz PA, McGee KP, Manduca A, Ehman RL. Magnetic resonance elastography as a method for the assessment of effective myocardial stiffness throughout the cardiac cycle. *Magn Reson Med* 2010;64:862–870.
- Kolipaka A, Aggarwal SR, McGee KP, Anavekar N, Manduca A, Ehman RL, Araoz PA. Magnetic resonance elastography as a method to estimate myocardial contractility. *J Magn Reson Imaging* 2012;36:120–127.
- Elgeti T, Beling M, Hamm B, Braun J, Sack I. Cardiac magnetic resonance elastography: toward the diagnosis of abnormal myocardial relaxation. *Invest Radiol* 2010;45:782–787.
- Sack I, Rump J, Elgeti T, Samani A, Braun J. MR elastography of the human heart: noninvasive assessment of myocardial elasticity changes by shear wave amplitude variations. *Magn Reson Med* 2009;61:668–677.
- Wassenaar PA, Eleswarpu CN, Schroeder SA, Mo XK, Raterman BD, White RD, Kolipaka A. Measuring age-dependent myocardial stiffness across the cardiac cycle using MR elastography: a reproducibility study. *Magn Reson Med* 2016;75:1586–1593.
- Glaser KJ, Manduca A, Ehman RL. Review of MR elastography applications and recent developments. *J Magn Reson Imaging* 2012;36:757–774.
- Meier C, Zwanger M, Feiweier T, Porter D. Concomitant field terms for asymmetric gradient coils: consequences for diffusion, flow, and echo-planar imaging. *Magn Reson Med* 2008;60:128–134.
- Jezzard P, Clare S. Sources of distortion in functional MRI data. *Hum Brain Mapp* 1999;8:80–85.
- Zhou XJ, Du YP, Bernstein MA, Reynolds HG, Maier JK, Polzin JA. Concomitant magnetic-field-induced artifacts in axial echo planar imaging. *Magn Reson Med* 1998;39:596–605.
- Kim YC, Nielsen JF, Nayak KS. Automatic correction of echo-planar imaging (EPI) ghosting artifacts in real-time interactive cardiac MRI using sensitivity encoding. *J Magn Reson Imaging* 2008;27:239–245.
- Reeder SB, Atalar E, Bolster BD Jr, McVeigh ER. Quantification and reduction of ghosting artifacts in interleaved echo-planar imaging. *Magn Reson Med* 1997;38:429–439.
- Pruessmann KP, Weiger M, Scheidegger MB, Boesiger P. SENSE: sensitivity encoding for fast MRI. *Magn Reson Med* 1999;42:952–962.
- Li H, Fox-Neff K, Vaughan B, French D, Szaflarski JP, Li Y. Parallel EPI artifact correction (PEAC) for N/2 ghost suppression in neuroimaging applications. *Magn Reson Imaging* 2013;31:1022–1028.
- Chen NK, Wyrwicz AM. Removal of EPI Nyquist ghost artifacts with two-dimensional phase correction. *Magn Reson Med* 2004;5:1247–1253.
- Bruder H, Fischer H, Reinfelder HE, Schmitt F. Image-reconstruction for echo planar imaging with nonequidistant k-space sampling. *Magn Reson Med* 1992;23:311–323.
- Saritas EU, Cunningham CH, Lee JH, Han ET, Nishimura DG. DWI of the spinal cord with reduced FOV single-shot EPI. *Magn Reson Med* 2008;60:468–473.
- Finsterbusch J. Improving the performance of diffusion-weighted inner field-of-view echo-planar imaging based on 2D-selective radio-frequency excitations by tilting the excitation plane. *J Magn Reson Imaging* 2012;35:984–992.
- Finsterbusch J. High-resolution diffusion tensor imaging with inner field-of-view EPI. *J Magn Reson Imaging* 2009;29:987–993.
- Ozaki M, Arai K, Miyoshi K, Worters PW, Banerjee S, Guidon A, Ikeda H, Kabasawa H. MR elastography using SS-SE-EPI with reduced FOV for kidney: preliminary study. In Proceedings of the 22nd Annual Meeting of ISMRM, Milan, Italy, 2014. Abstract 4234.
- Sui Y, Damen FC, Xie K, Zhou XJ. Image domain segmented diffusion imaging using a 2D excitation RF pulse for distortion reduction. In Proceedings of the 22nd Annual Meeting of ISMRM, Milan, Italy, 2014. Abstract 0608.
- Banerjee S, Nishimura DG, Shankaranarayanan A, Saritas EU. Reduced field-of-view DWI with robust fat suppression and unrestricted slice coverage using tilted 2D RF excitation. *Magn Reson Med* 2016;76:1668–1676.
- Reilly JP. Peripheral nerve stimulation by induced electric currents: exposure to time-varying magnetic fields. *Med Biol Eng Comput* 1989;27:101–110.
- Pauly J, Le Roux P, Nishimura D, Macovski A. Parameter relations for the Shinnar-Le Roux selective excitation pulse design algorithm [NMR imaging]. *IEEE Trans Med Imaging* 1991;10:53–65.
- Gomori JM, Holland GA, Grossman RI, Geftter WB, Lenkinski RE. Fat suppression by section-select gradient reversal on spin-echo MR imaging. Work in progress. *Radiology* 1988;168:493–495.
- Arani A, Glaser KL, Arunachalam SP, Rossman PJ, Lake DS, Trzasko JD, Manduca A, McGee KP, Ehman RL, Araoz PA. In vivo, high-frequency three-dimensional cardiac MR elastography: feasibility in normal volunteers. *Magn Reson Med* 2017;77:351–360.
- Arani A, Arunachalam SP, Chang ICY, et al. Cardiac MR elastography for quantitative assessment of elevated myocardial stiffness in cardiac amyloidosis. *J Magn Reson Imaging* 2017;46:1361–1367.
- King KF. ASSET-parallel imaging on the GE Scanner. 2nd International Workshop on Parallel MRI, Zurich, Switzerland; 2004. p. 15–17.
- Sinkus R, Tanter M, Xydeas T, Catheline S, Bercoff J, Fink M. Viscoelastic shear properties of in vivo breast lesions measured by MR elastography. *Magn Reson Imaging* 2005;23:159–165.
- Manduca A, Oliphant TE, Dresner MA, Mahowald JL, Kruse SA, Amromin E, Felmlee JP, Greenleaf JF, Ehman RL. Magnetic resonance elastography: non-invasive mapping of tissue elasticity. *Med Image Anal* 2001;5:237–254.
- Young PM, Mostardi PM, Glockner JF, Vrtiska TR, Macedo T, Haider CR, Riederer SJ. Prospective comparison of cartesian acquisition with projection-like reconstruction magnetic resonance angiography with computed tomography angiography for evaluation of below-the-knee runoff. *J Vasc Interv Radiol* 2013;24:392–399.
- McGarry MD, Van Houten EE, Perrinez PR, Pattison AJ, Weaver JB, Paulsen KD. An octahedral shear strain-based measure of SNR for 3D MR elastography. *Phys Med Biol* 2011;56:N153–N164.
- Arunachalam SP, Arani A, Baffour F, et al. Regional assessment of in vivo myocardial stiffness using 3D magnetic resonance elastography in a porcine model of myocardial infarction. *Magn Reson Med* 2018;79:361–369.
- Glaser KJ, Felmlee JP, Ehman RL. Rapid MR elastography using selective excitations. *Magn Reson Med* 2006;55:1381–1389.
- Stoeck CT, von Deuster C, Genet M, Atkinson D, Kozerke S. Second-order motion-compensated spin echo diffusion tensor imaging of the human heart. *Magn Reson Med* 2016;75:1669–1676.